High-throughput tracking of single yeast cells in a microfluidic imaging matrix

D. Falconnet[1,2], **A. Niemistö**[3], **R.J. Taylor**[1,2,3], **M. Ricicova**[1,2], **T. Galitski**[3], **I. Shmulevich**[3], and **C. L. Hansen**[1,2,3,4]

[1]Center for High-Throughput Biology, University of British Columbia, 2185 East Mall, Vancouver, B.C., Canada V6T-1Z4

[2]Department of Physics and Astronomy, University of British Columbia, 2185 East Mall, Vancouver, B.C., Canada V6T-1Z4

[3]Institute for Systems Biology, 1441 N. 34th Street, Seattle, WA 98103 USA

Summary

Time-lapse live cell imaging is a powerful tool for studying signaling network dynamics and complexity and is uniquely suited to single cell studies of response dynamics, noise, and heritable differences. Although conventional imaging formats have the temporal and spatial resolution needed for such studies, they do not provide the simultaneous advantages of cell tracking, experimental throughput, and precise chemical control. This is particularly problematic for systems-level studies using non-adherent model organisms such as yeast, where the motion of cells complicates tracking and where large-scale analysis under a variety of genetic and chemical perturbations is desired. We present here a high-throughput microfluidic imaging system capable of tracking single cells over multiple generations in 128 simultaneous experiments with programmable and precise chemical control. High-resolution imaging and robust cell tracking is achieved through immobilization of yeast cells using a combination of mechanical clamping and polymerization in an agarose gel. The channel and valve architecture of our device allows for the formation of a matrix of 128 integrated agarose gel pads, each allowing for an independent imaging experiment with fully programmable medium exchange via diffusion. We demonstrate our system in the combinatorial and quantitative analysis of the yeast pheromone signaling response across 8 genotypes and 16 conditions, and show that lineage-dependent effects contribute to observed variability at stimulation conditions near the critical threshold for cellular decision making.

Introduction

A central goal of systems biology is developing a quantitative and predictive understanding of how biomolecular networks process chemical information to direct appropriate cellular responses. A powerful approach to reverse engineering network function is the analysis of cellular response under a panel of defined genetic perturbations and a diversity of stimulation conditions. Owing to the facility of genetic manipulations, the availability of genome-wide gene deletion and GFP-fusion sets, and the wealth of biochemical data, yeast has emerged as a prototypical model of eukaryotic cell signaling. The recent application of genome-scale technologies for analysis of cellular response at the level of transcription, protein expression, and protein interaction has revealed the tapestry of network interactions that govern cellular growth and decision making.[1, 2] However, while such studies provide a

[4]Corresponding Author: C.L. Hansen, chansen@phas.ubc.ca.

global view of molecular response, they are typically limited by poor temporal and spatial resolution and provide only ensemble averaged population measurements, making them essentially blind to cell differences that arise from a combination of de-synchronization,[3] bistability,[4, 5] and stochastic variations in expression.[6-9] Flow cytometry allows for high-throughput studies of heterogeneity in single cells but does not provide information on subcellular localization or morphology, and does not allow for the tracking of cells through time.[7, 10] The latter point is particularly important in understanding differences that may arise through unique past cell histories or lineage-dependent differences.

The combination of genetically encoded fluorescent reporters and microscopy has emerged as the premier tool for single-cell studies of biological networks [11-14] and has been used to dissect heterogeneity associated with emergent network properties including bet-hedging[10, 15], adaptation,[16] and memory.[17-19] Conventional formats for time-lapse imaging of yeast use the immobilization of cells between a cover slip and an agar pad.[5, 20] While simple to implement, this method has significant limitations including the inability to exchange nutrients over time, and limited throughput in terms of the numbers of strains and media conditions that may be studied in a single experiment. In addition, the accumulation of metabolites, depletion of nutrients, and the growth of cells in multiple layers limits the duration of experiments, confounding long-time studies of adaptation or cell-lineage effects over multiple generations. Thus there is a need for high-throughput technology capable of long-term tracking of single cells from multiple strains and over an array of controllable chemical conditions.

Microfluidic technologies offer advantages of both scalability and precise fluid control and have recently emerged as a method for scalable imaging studies of cells in precisely controlled and changing microenvironments.[4, 18, 21-28] In particular, the large-scale integration of microfluidic valves using Multilayer Soft Lithography (MSL) has been broadly applied to studies on bacteria, yeast or mammalian cells under chemostatic[22, 25, 27, 29] or chemodynamic conditions.[21, 30, 31] We have recently reported the development of a high-throughput microfluidic imaging platform based on MSL technology for the study of yeast signaling. This previously reported device features an imaging matrix for the simultaneous analysis of 8 genotypes under 32 time-varying chemical sequences in a total of 256 perfusion chambers.[18] Within each perfusion chamber, cells were immobilized by trapping them between partially closing "sieve"-valves, thereby allowing for media exchange around non-adherent yeast. Although this platform allowed for precise and high-throughput comparisons of dynamic responses and cell to cell variability across genotypes, it did not support the tracking of cells through time. This limitation is due to transient flows during perfusion that result in the motion of cells within chambers, making automated tracking of cells difficult or impossible. In addition, the small dimensions of the perfusion chambers result in confluence at approximately 300 cells, imposing a practical limit on the duration of experiments. Here we describe a technology that addresses all these limitations to combine the high-throughput and chemical control of microfluidics with long-term tracking of cells and lineages. This system is capable of running simultaneously, and in an unattended manner, 128 different experiments on tens of thousands of immobilized non-adherent single yeast cells exposed to various pre-programmed chemical perfusion schemes. We demonstrate our microfluidic technology in the analysis of the pheromone induced mitogen-activated protein kinase (MAPK) signaling network in Saccharomyces cerevisiae.

Results

Microfluidic chip overview and operation

Our device features a matrix architecture designed to test different genotypes, loaded through 8 columns, against programmable chemical sequences delivered through the 16

rows for a total of 128 simultaneous live cell imaging experiments (Figure 1a, 1b). Combining the scalability and medium exchange capabilities of microfluidics with long-term tracking of specific single cells through time requires methods for the immobilization of cells. Previous approaches for immobilization of non-adherent cells include mechanical clamping under a permeable membrane[32, 33], adsorption to channel walls [15, 34], and mechanical trapping by microfabricated constrictions.[35-37]

Here we developed and integrated a scalable and robust alternative method that combines mechanical clamping with *in situ* polymerization to allow for the robust immobilization of cells in an array of 128 chambers (Figure 1b) located at the intersections of 8 columns and 16 rows. Valve actuation sequences for the loading and perfusion of cells are illustrated in Figure 1c. Prior to loading the device each strain is suspended in liquid medium containing un-polymerized low melting temperature agarose. All chamber diffusion valves are closed during loading and each column of the array is isolated by actuation of column valves, creating a serpentine fluidic path through which unique strains are loaded. Chamber compartmentalization valves are then actuated together with row valves to isolate the liquid gel cell suspension in each chamber and to isolate the rows for perfusion. The chambers, which are designed to have a height smaller than the yeast cells, are inflated during this loading process and subsequently relax, pressing the cells into a monolayer on the glass substrate. The column valves are then opened and the rows are flushed with medium, leaving gel only in the imaging chambers. The device is then cooled to 4°C by placing it in contact with a cooled block. Polymerization of the gel suppresses any convection in the chambers that would otherwise result in the escape of new daughter cells which are smaller than the adjacent mother cells. In addition, this method is robust to pressure fluctuations (caused by valve actuation), or pressure variations resulting from flow across the array, enabling long-term imaging with near perfect cell immobilization. After loading, cells are perfused for 3 hours with medium in order to eliminate possible stress responses arising from cooling or from the injection of cells into the device. The on-chip division time for yeast at 25°C in SCD media was measured to be approximately 220 minutes under conditions of both continuous perfusion and the slowest frequency of periodic perfusion used. Further, experiments show that varying gel density has no effect on cell division rates or on cell response to pheromone.

On-chip fluid handling allows for precise and unattended perfusion of each row with arbitrary chemical sequences over 24 hours. Reagents are delivered to the array from a bank of 8 chemical inlet ports (Figure 1b, region 3). A fluidic multiplexer allows for perfusion of each row of the matrix (Figure 1b, region 5) with programmable concentrations and sequences of medium conditions created by the on-chip metering of relative stock reagents using varying numbers of cycles of an integrated peristaltic pump, each delivering approximately 150 pL of solution (Supplementary Table 2). For example a 22 nM solution is prepared by sequential injection of two pump cycles of 100 nM stock solution, two cycles of 10 nM stock solution, and 6 cycles of 0 nM stock solution to define a combined 1.5 nL "fluidic slug" with average α-factor concentration of 22 nM. The process is continuously repeated for 1min per row. Replacing the whole volume of a perfusion channel requires approx. 35 s. Taylor dispersion of reagents during transport from the chemical inlets to the array results in complete mixing. Measurements of on-chip mixing of 16 different fluorescein concentrations from 3 stock solutions (1×, 10×, 100×) show excellent linearity ($R^2 = 0.9996$) and spatial uniformity across the entire agar-filled chamber array (Figure 1e).

The short characteristic length scales of our microfabricated chambers allow for efficient exchange of medium, nutrients, and metabolites via diffusion conduits that connect the imaging chambers to the adjacent channels that feed each row. Assuming a characteristic distance of approximately 400 microns, and a characteristic small molecule diffusion

constant of $\sim 0.5 \times 10^{-9}$ m^2/s, we estimate a mixing time of $\tau \sim d^2/D \sim (400 \times 10^{-6})^2/0.5 \times 10^{-9} \sim 5$ minutes, which is confirmed by measurements of the kinetics of equilibration of fluorescein in agarose filled chambers (Figure 1f). This exchange time is comparable to the time required to image the full microfluidic array (~ 10 minutes) and is well-suited to prolonged experiments requiring the modulation of chemical conditions on time-scales much shorter than the cell cycle. In cases where faster solution exchange is needed more rapid exchange can be achieved by reducing the chamber width or widening and shortening the diffusion channels connecting the chambers to the perfusion channels.

The combination of cellular confinement and periodic perfusion allows for extended imaging studies over multiple generations that are difficult to implement in conventional formats. During each device run, automated microscopy generates 128 time-lapse image sets with temporal resolution of 10 minutes, limited only by the time required to image the complete array in both fluorescent and brightfield mode. Continuous perfusion of the chambers supports the growth of cells to high density (Figure 2a,b) by replenishment of nutrients and removal of waste. Each imaging chamber has dimensions of $684 \times 260 \times 4.4$ μm^3 and can host over 6,000 cells corresponding to 8.5×10^9 cells/ml. By comparison, a yeast culture typically reaches stationary phase at about 2-3 10^8 cells/ml due to nutrient limitation. During imaging experiments yeast are confined by the chamber height to grow as a monolayer in a single focal plane over multiple generations. The bottom of the imaging chamber is sealed with a microscope slide or cover slip, so that the device is compatible with any inverted microscope and is suitable for high resolution imaging using low working distance (high numerical aperture) objectives (inset, Figure 2c). In situations where high resolution and fluorescence collection efficiency is not required, the robust long-term imaging of large area arrays is facilitated by using air-coupled objectives. A representative fluorescent image (40×, 0.6NA) showing sub-cellular localization of STE20-GFP in cells exposed to pheromone is shown in Figure 2c.[38]

High-throughput Analysis of MAPK Signaling in Yeast

We demonstrated the throughput, control, and precision of our approach in the analysis of the yeast pheromone mating response. The pheromone response is a well-characterized signaling pathway that serves as an archetypical model of the highly conserved mitogen activated protein kinase (MAPK) signaling cascades in eukaryotic cells. MAPK signaling governs cellular response to a staggering range of stimuli including growth factors, cytokines, hormones, cellular adhesion, stress, and nutrient conditions.[39] In yeast cells MAPK signaling is used for sexual reproduction between haploid cells of type **a** and **α**. Mating response is induced by the binding of a soluble pheromone peptide via the membrane-localized G-protein-coupled receptor Ste2 which initiates a phosphorylation cascade, ultimately activating the expression of about 200 genes and culminating in growth arrest and formation of a pointed extension (a shmoo) towards the pheromone gradient. Although this pathway has been the subject of intense study and is likely the most well-characterized of all MAPK networks, the vast majority of analysis has been qualitative and there remain many open questions on how network architecture gives rise to emergent properties including cross-talk and specificity, filtering, adaptation, memory, and cellular variability.[40-43]

Using a single device run we monitored the response of over 60,000 individual yeast cells from 8 strains (wildtype and 7 deletion mutants) exposed to 16 different α-factor concentrations (Supplementary Table 2). Brightfield and fluorescent images were collected at 20 min time resolution to capture response dynamics and while avoiding unnecessary photo-damage of cells. To correlate mating-pathway activity with morphological phenotype we transformed the strains with a GFP reporter under control of a mating-specific promoter (Supplementary methods). During a 24h experiment over 40,000 bright field differential

interference contrast and fluorescence images were recorded, representing ~4 million cell measurements stored in 100 Gb of raw image data. To deal with this volume data we built a custom image analysis pipeline in MATLAB (The Mathworks, Inc., Natick, MA) implementing the following tasks: (i) segmentation and tracking of cells, (ii) calculation of total fluorescence in each cell, (iii) calculation of statistics across all cells and experimental conditions and, (iv) generation of figures, movies, and tables to present time-course and steady-state data (Supplementary Methods). In particular, the generation of movies for each chamber enables rapid qualitative analysis of each experiment in order to guide subsequent data analysis and hypothesis testing (Supplemental Videos 1,2,3).

Parallel analysis of multiple strains and conditions allows for the rapid collection of unified data sets that facilitate the precise comparison of response kinetics and noise within a population, between different experimental conditions, and across varying genotypes. Such analysis is particularly important for studying subtle differences that may be obscured by systematic variations between experiments. For example, data from a single experimental run comparing the response of various genotypes to sustained pheromone stimulation at varying concentration is shown in Figure 3. The kinetics of GFP expression response in wild type cells (GFP normalized to the cell volume) is shown in Figure 3a. Approximately 300 min after induction the population reached a steady state GFP expression with approximately a 12 fold increase over basal levels. We observe pronounced noise in network response[3, 7, 44-49] with a coefficient of variation of 0.3. The time-dependent dose response of wild type cells is represented by a two-dimensional plot of GFP expression under 16 pheromone concentrations over 600 minutes (Figure 3b). Cells show a subtle response at alpha-factor concentrations as low as 1nM, and exhibit a saturated response under stimulation at concentrations in the range of 22-30 nM. Below saturation, the response was found to be monotonically graded with pheromone concentration.

The parallel analysis of multiple strains under identical experimental conditions allows for precise characterization of the effect of genetic perturbations to network response (Figures 3c-i). We observe that under constant stimulation that ptp2Δ, msg5Δ and kss1Δ deletion strains are hyper-sensitive (in increasing order) while ste50Δ, far1Δ, slt2Δ and fus3Δ deletion strains are hypo-sensitive (in decreasing order) with respect to wild-type, consistent with previous high-throughput and focused studies.[3, 4, 18, 50] In addition, analysis under constant and finely varied concentrations of pheromone reveals different response saturation thresholds amongst mutants. For example, slt2Δ saturates at alpha-factor concentrations as low as 10 nM while ste50Δ does not reach steady state within the time of the experiment.

Single-cell tracking reveals heterogeneous decision making

Yeast cells are known to adopt various morphologies depending on their surrounding pheromone concentration.[18, 51, 52] While the noise in PRE-dependent gene expression is substantial at all pheromone concentrations, the observed morphology of yeast at both high (schmoo form) and low (yeast form) pheromone concentrations is highly uniform across each population. However, the coexistence of multiple morphologies is observed at intermediate concentrations of pheromone, suggesting that cells undergo a switch-like decision at a threshold pheromone concentration that may vary between cells. Between 0-3 nM wild-type cells displayed a yeast morphology while between 4 and 8 nM an increasing fraction of the population was observed to display an elongated morphology (Supplementary Figure 1). This transition culminated in a complete switching from budding yeast to the elongated phenotype at concentration above 8 nM, and was accompanied by complete growth arrest. When the cells were exposed with 30 nM or higher they adopted the more common shmooing phenotype characterized by one or more short and pointed projections. Interestingly, single cell tracking experiments suggest that this observed variability is not random but is rather correlated with cell lineage (Figure 4). A representative time sequence

of heterogeneous morphological response in two colonies of wild-type cells exposed to 5 nM α-factor is shown in Figure 4d. Colonies are separated by a distance of approximately 30 microns and are hence exposed to identical chemical conditions. Despite identical stimulation and genotype, one population (red) undergoes growth arrest and cellular volume increase while the adjacent population (green) is apparently insensitive to pheromones and continues to divide.

Measurements of GFP expression reporting on the pheromone pathway activity provide complementary information to the bright field images, suggesting a direct correlation between growth arrest and elongation with higher GFP expression (Figure 4c). To accurately quantify the GFP expression in each cell and over time we built a cell tracking algorithm which labels each cell (Figure 4b) and allows plotting their respective time-lapse gene expression profiles as shown in Figure 4e. Cells undergoing growth arrest (red) display a strong increase in GFP expression (12 fold over basal levels) while dividing cells (green) only show a moderate GFP response (5 fold over basal levels). This observation suggests that pathway response is graded and that cells exhibit varying pathway sensitivity which is correlated with lineage. At intermediate α-factor concentrations this inherited variability in sensitivity manifests itself as a heterogeneous and switch-like morphological response of the population, causing only a subset of cells to commit to growth arrest and morphological transition. The ability to keep cells growing as a monolayer allows for reconstruction of lineages from time-lapse images (Figure 4f). We are currently extending our automated cell tracking algorithms for high-throughput lineage tracking, a task that is facilitated by the use of fluorescent budneck markers for connecting mother cells to their progeny.[32] This approach will, for the first time, enable the rigorous correlation of cellular response as a function of lineage over large populations of cells from varying genotypes and under changing environmental conditions. Such studies should open new avenues for exploring cell heterogeneity and potential heritable effects in signaling.

For instance, here we show that high-throughput single analysis of the mating response under finely graded and constant concentrations of pheromone reveals a strong heritable contribution to observed heterogeneity in morphological switching and gene expression response. We propose that this is not a specific property of the mating response, but rather a general property of any switch-like behavior near a critical threshold of stimulation. Any all-or-nothing cellular decision, such as the decision to growth arrest and mate, must be tightly regulated to avoid costly and nonproductive responses. This regulation is achieved through complex signaling network architecture to enforce a well-defined transition threshold. However, signaling networks are subject to noise arising from stochastic variations in the abundance of signaling molecules and transcripts, resulting in unique thresholds for each cell. Progeny inherit the state and concentrations of proteins and transcripts present in the mother and hence exhibit thresholds that are correlated over generations. Thus, analysis of any cellular decision making near critical concentrations of stimulant may be generally expected to elicit incomplete population response that reflects stochastic differences in signaling network state passed from one generation to the next. Thus we contend that this mechanism may constitute an important source of cell-cell variability near any switching transition.

Experimental

Chip fabrication—Poly-dimethylsiloxane (PDMS, RTV615 manufactured by General Electric, CT) microfluidic devices were fabricated by replica molding from micromachined masters using multilayer soft lithography as previously described.[24, 53, 54] Devices feature 2-layers with the top layer containing channels used for pneumatic valving and the bottom layer containing flow channels and imaging chambers. Device design was completed using

AutoCAD software (Autodesk, Inc., San Rafael, CA) and printed on 20,000 dot per inch resolution transparency masks (Cad/Art Services, Bandon, Oregon). Master negative molds were fabricated by standard photolithography techniques on 4 inch (101.6 mm) silicon wafers (Silicon Quest International, Santa Clara, CA). The flow layer consisted of two feature types: 4.4 μm high rectangular cell microchambers, and 9 μm high rounded flow channels. The rounded channel cross-sections were obtained with by placing the wafer on a 130°C for 30 min. Each cell microchamber had a volume of 0.71 nL with dimensions 684 × 260 × 4.4 μm^3. The 4.4 μm and 9 μm layers were made using negative (SU8-5, Microchem Corp., Newton, MA) and positive photoresist (SPR220-7, Microchem Corp) respectively. The control master was a single layer mold consisting of 25 μm high squared features made with SU8-2025 negative photoresist (Microchem Corp.). Resist processing was performed according to the manufacturer's specifications. The bottom layer of the device was sealed by covalent bonding to a 0.7 mm low auto-fluorescence glass slides (borofloat 33, S.I. Howard Glass Co., Inc. MA) by a 10 s O_2-plasma surface activation followed by baking for 15h at 80°C.

Segmentation and tracking algorithm—Cell segmentation was performed using only bright-field images. Focus was adjusted during image capture to ensure yeast cell walls were clearly visible as dark continuous borders. The local mean and variance were calculated for each pixel of the image using a small local neighborhood, and those pixels for which the local mean was below a threshold and the local variance was above a threshold were marked as cell wall pixels.[55] Subsequently, a mask of cell areas was obtained by thresholding the local variance image with a threshold found with the help of Otsu's method,[56] followed by a series of operations based on mathematical morphology. Initially recognized cell walls were then removed from the mask and cells that were grouped together were separated by a watershed method (Supplementary Methods). The cell tracking was based on minimizing the sum of Euclidean distances between cells from each image frame at time point t with cells from the image frame at time point t-1. If the number of cells at each time point was the same, the solution to this assignment problem giving the smallest total cost (sum of distances between cells) could be readily found by the classic Hungarian algorithm.[57] When this was not the case, due to cell division or segmentation errors, we applied a modified assignment method based on the Hungarian algorithm (see supplementary notes for details).

Additional methods—Description of the yeast constructs as well as further details on chip fabrication and operation are available in Supplementary Methods.

Conclusion

We have developed a microfluidic chip that addresses major limitations in live-cell imaging studies of signaling. The unique combination of experimental throughput, single cell tracking, chemical control, and quantitative image analysis is ideally suited to tackling fundamental questions including mechanisms of signaling specificity and cross-talk, cellular filtering, and the origin of heritable differences in isogenetic populations. As a demonstration we report here new observations of cell-to-cell variability in pheromone response that suggest non-genetic inheritance as a contributing source to observed heterogeneous response in an isogenic population of cells. We contend that this and similar technology will become a premier tool for the quantitative analysis of natural and synthetic biological networks, ultimately providing stringent tests for the development and testing of *in silico* models and leading to predictive understanding of complex cellular decision making.

Supplementary Material

Refer to Web version on PubMed Central for supplementary material.

Acknowledgments

References

1. Roberts CJ, Nelson B, Marton MJ, Stoughton R, Meyer MR, Bennett HA. Science. 2000; 287:873–880. [PubMed: 10657304]

2. Eisen MB, Spellman PT, Brown PO, Botstein D. Proc Natl Acad Sci U S A. 1998; 95:14863–14868. [PubMed: 9843981]

3. Colman-Lerner A, Gordon A, Serra E, Chin T, Resnekov O, Endy D, Pesce CG, Brent R. Nature. 2005; 437:699–706. [PubMed: 16170311]

4. Paliwal S, Iglesias PA, Campbell K, Hilioti Z, Groisman A, Levchenko A. Nature. 2007; 446:46–51. [PubMed: 17310144]

5. Kaufmann BB, Yang Q, Mettetal JT, van Oudenaarden A. PLoS Biol. 2007; 5:1973–1980.

6. Shahrezaei V, Ollivier JF, Swain PS. Mol Syst Biol. 2008; 4:196. [PubMed: 18463620]

7. Ansel J, Bottin H, Rodriguez-Beltran C, Damon C, Nagarajan M, Fehrmann S, Francois J, Yvert G. PLoS Genet. 2008; 4:e1000049. [PubMed: 18404214]

8. Eldar A, Elowitz MB. Nature. 2010; 467:167–173. [PubMed: 20829787]

9. To TL, Maheshri N. Science. 2010; 327:1142–1145. [PubMed: 20185727]

10. Acar M, Mettetal JT, van Oudenaarden A. Nat Genet. 2008; 40:471–475. [PubMed: 18362885]

11. Gordon A, Colman-Lerner A, Chin TE, Benjamin KR, Yu RC, Brent R. Nat Methods. 2007; 4:175–181. [PubMed: 17237792]

12. Fricker M, Runions J, Moore I. Annu Rev Plant Biol. 2006; 57:79–107. [PubMed: 16669756]

13. Shaner NC, Lin MZ, McKeown MR, Steinbach PA, Hazelwood KL, Davidson MW, Tsien RY. Nat Methods. 2008 advanced online publication.

14. Muzzey D, van Oudenaarden A. Annu Rev Cell Dev Biol. 2009; 25:301–327. [PubMed: 19575655]

15. Nachman I, Regev A, Ramanathan S. Cell. 2007; 131:544–556. [PubMed: 17981121]

16. Zhou J, Arora M, Stone D. Cell Biochem Biophys. 1999; 30:193–212. [PubMed: 10356642]

17. Acar M, Becskei A, van Oudenaarden A. Nature. 2005; 435:228–232. [PubMed: 15889097]

18. Taylor RJ, Falconnet D, Niemisto A, Ramsey SA, Prinz S, Shmulevich I, Galitski T, Hansen CL. Proc Natl Acad Sci U S A. 2009; 106:3758–3763. [PubMed: 19223588]

19. Gordon AJ, Halliday JA, Blankschien MD, Burns PA, Yatagai F, Herman C. PLoS Biol. 2009; 7:e44. [PubMed: 19243224]

20. Bean JM, Siggia ED, Cross FR. Mol Cell. 2006; 21:3–14. [PubMed: 16387649]

21. Gomez-Sjoberg R, Leyrat AA, Pirone DM, Chen CS, Quake SR. Anal Chem. 2007

22. Balagadde FK, You LC, Hansen CL, Arnold FH, Quake SR. Science. 2005; 309:137–140. [PubMed: 15994559]

23. Thorsen T, Maerkl SJ, Quake SR. Science. 2002; 298:580–584. [PubMed: 12351675]

24. Melin J, Quake SR. Annu Rev Biophys Biomol Struct. 2007; 36:213–231. [PubMed: 17269901]

25. King KR, Wang SH, Irimia D, Jayaraman A, Toner M, Yarmush ML. Lab Chip. 2007; 7:77–85. [PubMed: 17180208]

26. Bennett MR, Hasty J. Nat Rev Genet. 2009; 10:628–638. [PubMed: 19668248]

27. Groisman A, Lobo C, Cho HJ, Campbell JK, Dufour YS, Stevens AM, Levchenko A. Nat Methods. 2005; 2:685–689. [PubMed: 16118639]

28. Chen D, Du W, Liu Y, Liu W, Kuznetsov A, Mendez FE, Philipson LH, Ismagilov RF. Proc Natl Acad Sci U S A. 2008; 105:16843–16848. [PubMed: 18974218]

29. Balagadde FK, You LC, Arnold FH, Quake SR. Biophys J. 2005; 88:519A–519A.

30. Bennett MR, Pang WL, Ostroff NA, Baumgartner BL, Nayak S, Tsimring LS, Hasty J. Nature. 2008; 454:1119–1122. [PubMed: 18668041]

31. Cheong R, Wang CJ, Levchenko A. Mol Cell Proteomics. 2009; 8:433–442. [PubMed: 18953019]

32. Charvin G, Cross FR, Siggia ED. PLoS ONE. 2008; 3:e1468. [PubMed: 18213377]

33. Mirzaei M, Pla-Roca M, Safavieh R, Nazarova E, Safavieh M, Li H, Vogel J, Juncker D. Lab Chip. 2010; 10:2449–2457. [PubMed: 20714499]

34. Mettetal JT, Muzzey D, Gomez-Uribe C, van Oudenaarden A. Science. 2008; 319:482–484. [PubMed: 18218902]

35. Lee PJ, Helman NC, Lim WA, Hung PJ. BioTechniques. 2008; 44:91–95. [PubMed: 18254385]

36. Bennett MR, Pang WL, Ostroff NA, Baumgartner BL, Nayak S, Tsimring LS, Hasty J. Nature. 2008

37. Rowat AC, Bird JC, Agresti JJ, Rando OJ, Weitz DA. Proc Natl Acad Sci U S A. 2009; 106:18149–18154. [PubMed: 19826080]

38. Yu L, Qi M, Sheff MA, Elion EA. Mol Biol Cell. 2008; 19:1739–1752. [PubMed: 18256288]

39. Pearson G, Robinson F, Gibson TB, Xu BE, Karandikar M, Berman K, Cobb MH. Endocr Rev. 2001; 22:153–183. [PubMed: 11294822]

40. Bardwell L. Peptides. 2005; 26:339–350. [PubMed: 15690603]

41. Sabbagh W Jr, Flatauer LJ, Bardwell AJ, Bardwell L. Mol Cell. 2001; 8:683–691. [PubMed: 11583629]

42. Madhani HD, Styles CA, Fink GR. Cell. 1997; 91:673–684. [PubMed: 9393860]

43. Yu RC, Pesce CG, Colman-Lerner A, Lok L, Pincus D, Serra E, Holl M, Benjamin K, Gordon A, Brent R. Nature. 2008; 456:755–761. [PubMed: 19079053]

44. Suel GM, Kulkarni RP, Dworkin J, Garcia-Ojalvo J, Elowitz MB. Science. 2007; 315:1716–1719. [PubMed: 17379809]

45. Mettetal JT, Muzzey D, Pedraza JM, Ozbudak EM, van Oudenaarden A. Proc Natl Acad Sci U S A. 2006; 103:7304–7309. [PubMed: 16648266]

46. Pedraza JM, van Oudenaarden A. Science. 2005; 307:1965–1969. [PubMed: 15790857]

47. Shedden K, Cooper S. Nucleic Acids Res. 2002; 30:2920–2929. [PubMed: 12087178]

48. Longo D, Hasty J. Nat Chem Biol. 2006; 2:181–182. [PubMed: 16547478]

49. Newman JRS, Ghaemmaghami S, Ihmels J, Breslow DK, Noble M, DeRisi JL, Weissman JS. Nature. 2006; 441:840–846. [PubMed: 16699522]

50. Chen RE, Thorner J. Biochim Biophys Acta. 2007; 1773:1311–1340. [PubMed: 17604854]

51. Hao N, Nayak S, Behar M, Shanks RH, Nagiec MJ, Errede B, Hasty J, Elston TC, Dohlman HG. Molecular Cell. 2008; 30:649–656. [PubMed: 18538663]

52. Erdman S, Snyder M. Genetics. 2001; 159:919–928. [PubMed: 11729141]

53. Unger MA, Chou HP, Thorsen T, Scherer A, Quake SR. Science. 2000; 288:113–116. [PubMed: 10753110]

54. Hansen CL, Sommer MO, Quake SR. Proc Natl Acad Sci U S A. 2004; 101:14431–14436. [PubMed: 15452343]

55. Niemisto A, Nykter M, Aho T, Jalovaara H, Marjanen K, Ahdesmaki M, Ruusuvuori P, Tiainen M, Linne ML, Yli-Harja O. EURASIP J Bioinform Syst Biol. 2007:46150. [PubMed: 18354733]

56. Otsu N. Ieee Transactions on Systems Man and Cybernetics. 1979; 9:62–66.
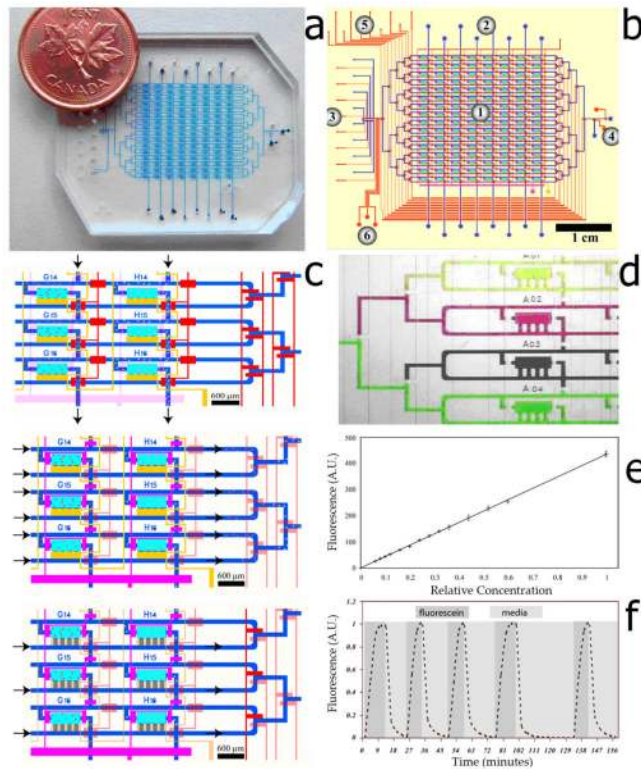
57. Kuhn HW. Naval Research Logistics. 2005; 52:7–21.

Figure 1. Microfluidic chip design and operation
(a) Image of microfluidic device. A Canadian penny has been included for scale. **(b)** Working area of microfluidic device showing (1) array of 128 imaging chambers (8 columns * 16 rows), (2) column inlets for loading different strains, (3) 8 chemical inlets controlled by independent valves, (4) outlet ports, (5) fluidic multiplexer to deliver reagents to specified rows, (6) integrated peristaltic pump for on-chip formulation of stock reagents. **(c)** Cell loading and immobilization. Top: Cell suspension containing low melting temperature liquid agarose gel and media are introduced through column flow channels (blue) which are separated by the actuation of column valves (red) to prevent cross contamination of strains. Diffusion valves (yellow) are closed while the row valves (pink) are open. Middle: Actuation of row valves stops flow of cells and isolates each chamber. Column valves are released to flow media along rows, flushing excess cells and agarose to the outlet. Bottom: The chip is cooled for 3 min at 4 C to gel the agarose. Diffusion valves are opened to initiate diffusive exchange between medium in row channels and imaging chambers. Each row has a dedicated waste channel above the chambers for the priming of rows prior to initiating diffusion, thereby eliminating possible contamination from adjacent rows. **(d)** Optical micrograph showing the programmable and independent sequential perfusion of adjacent rows with 4 solutions of food dye. **(e)** Programmable on-chip mixing of 3 fluorescein stock solutions (1×, 10×, 100×) to create 16 concentrations. Each data point corresponds to the mean fluorescence of the 8 chambers on each row. Y-error bars represent standard deviations across the 8 chambers of each row. Measurements were taken at edge of the chamber furthest away from the diffusion channel and therefore reflect the longest possible diffusion time within chambers. **(f)** Temporal modulation of the chemical environment demonstrated by constant perfusion with repeated pulses alternating between medium and fluorescein. Greater than 95% equilibration is achieved within 9 minutes. Note that data presented in panels 1e and 1f was taken from chambers filled with polymerized agarose as in biological experiments.
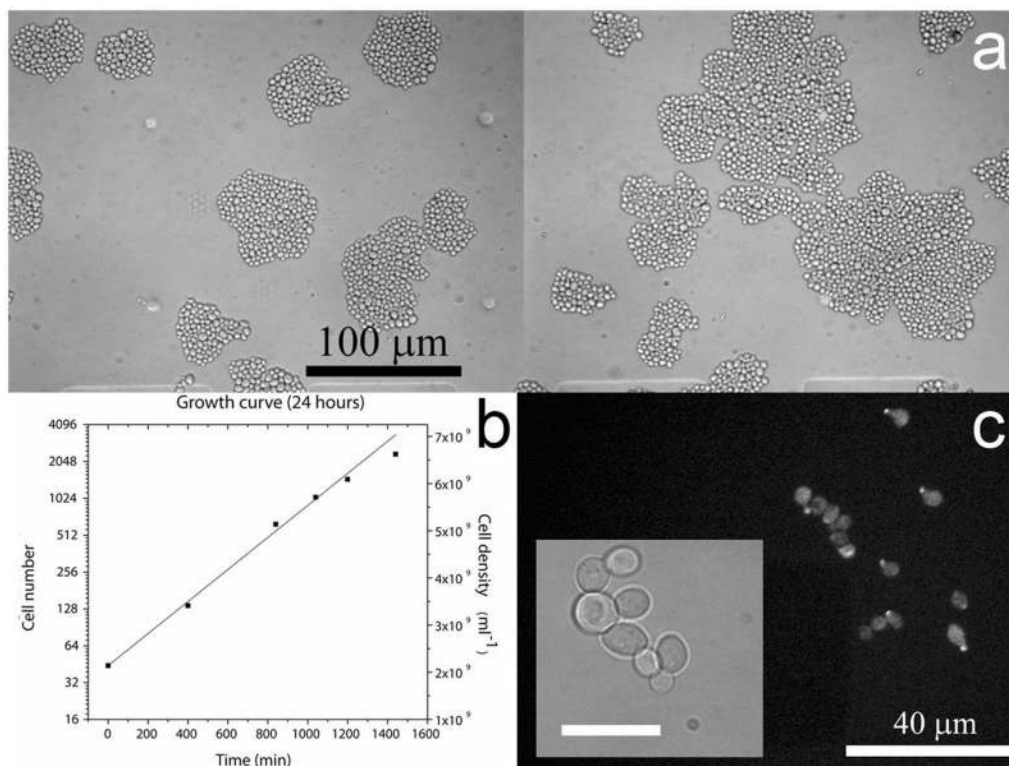
Figure 2. Cell growth and imaging quality
(a) Bright field images of one imaging chamber captured in two fields of view taken after 24 hours growth in synthetic media. Image taken using a 40× long working distance air objective (NA=0.6) **(b)** Growth curve of cells in a chamber over 24 hours showing growth to high density (3.5×10^9 cells/ml) under periodic diffusive exchange of nutrients and metabolites. **(c)** Compatibility of imaging platform with high-resolution microscopy. Fluorescent images taken with a 40× air objective (NA=0.6) show localization of a STE20-GFP fusion protein at the shmoo tip after exposure to pheromone. Inset shows a separate brightfield image taken using a 100× oil immersion objective (NA=1.3), demonstrating that the device is compatible with high resolution microscopy. Scale bar is 8 μm.
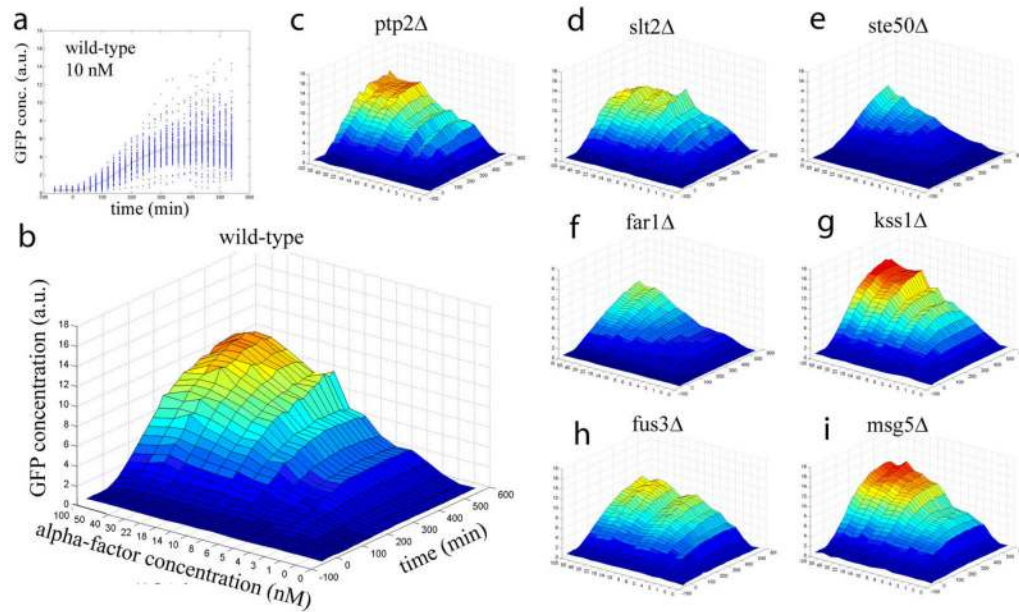
Figure 3. Time-course pheromone dose response across multiple genotypes
(a) Data from one of 128 chambers showing variation of GFP expression for wild-type cells subject to constant 10 nM α-factor stimulation. Each data point represents one time-point for a single cell measured every 20 min over 9 h. **(b)** Mean expression data from one column of the device presented as a surface plot of GFP concentration as a function of time and α-factor concentration. **(c)-(i)** GFP expression surface plots for seven mutants studied on the same device. Each surface response plot represents approximately 200,000 individual data points.
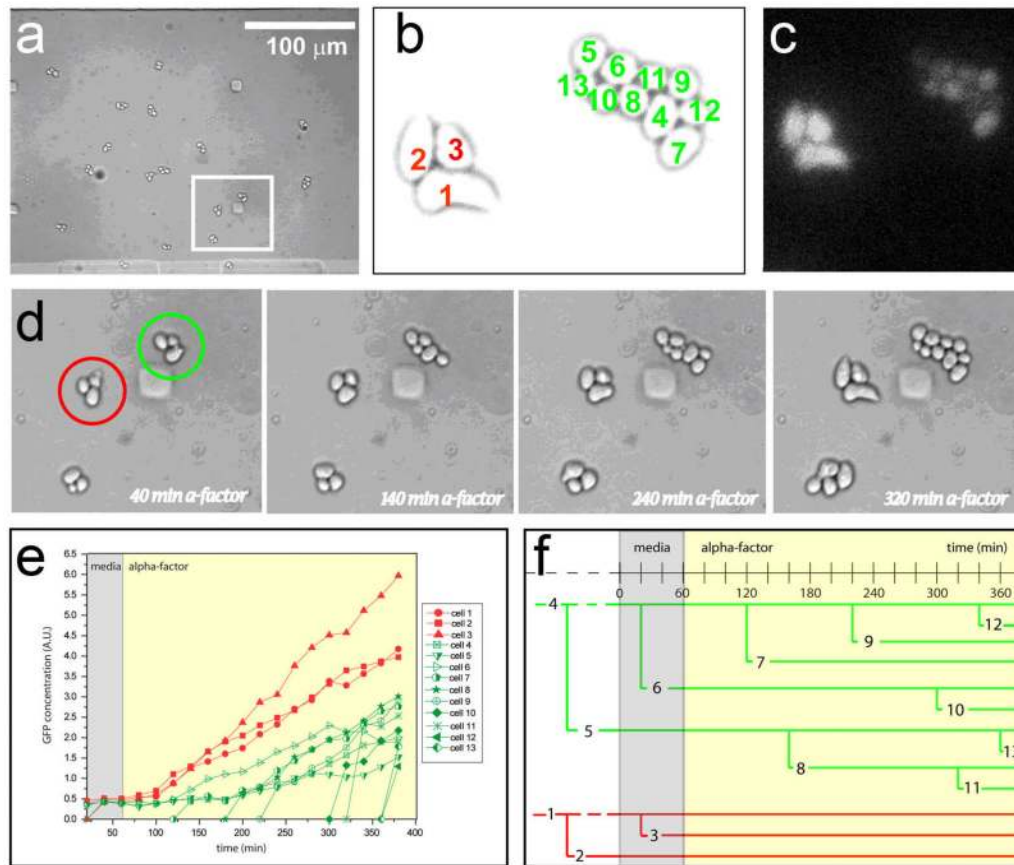
Figure 4. Evidence of a heritable threshold for morphological switching

(**a**) Bright field image of colonies of bar1Δ cells after 40 minute exposure to 5nM α-factor in microfluidic chamber. (**b**) Close-up of upper two colonies from inset of panel **a** after 320 minute exposure to 5nM α-factor. Automated cell-tracking assigns a unique label to each cell to allow correlation of lineage, morphology, budding pattern and gene expression. (**c**) Fluorescent image of GFP expression in colonies from panel **b** showing lineage-dependent sensitivity to pheromone. (**d**) Time-lapse sequence of colonies highlighted in panel **a** showing the evolution of variability in morphological response to pheromone response. The red population undergoes growth arrest and displays an elongated phenotype while the green keeps budding over multiple generations. (**e**) EGFP concentration in each cell reporting the pheromone pathway activity. New lines starting at a zero value for GFP correspond to newborn cells. Plotted gene expression is normalized to cell volume and therefore represents an estimate of GFP concentration. (**f**) Lineage tree with time scale for both populations.